Nuclear Engineering and Technology 58 (2026) 104252

Contents lists available at ScienceDirect

Nuclear Engineering and Technology

journal homepage: www.elsevier.com/locate/net

Original Article

Electrorefining of HANA-4 cladding scrap in LiCl-KCl salts for volumetric decontamination of irradiated cladding containing Nb-94

Sungjune Sohn [a], Jungho Hur [b], Jaeyeong Park [c,*], Pyeonghwa Kim [d], Il Soon Hwang [d,e]

[a] Nuclear Facility Cleanup Technology Division, Korea Atomic Energy Research Institute, 989-111 Daedeok-daero, Yuseong-gu, Daejeon, 34057, Republic of Korea
[b] Fuel Cycle Technology Strategy Section, Korea Atomic Energy Research Institute, 989-111 Daedeok-daero, Yuseong-gu, Daejeon, 34057, Republic of Korea
[c] Department of Nuclear Engineering, Ulsan National Institute of Science and Technology, 50 UNIST-gil, Ulju-gun, Ulsan, 44919, Republic of Korea
[d] Department of Nuclear Engineering, Seoul National University, 1 Gwanak-ro, Gwanak-gu, Seoul, 08826, Republic of Korea
[e] MicroURANUS Corp., 50 UNIST Road, Eonyang-eup, Ulju-gun, Ulsan, 44919, Republic of Korea

ARTICLE INFO

Keywords:
Zr-Nb alloy
Volumetric decontamination
Electrorefining
Molten salt
Nb electrochemistry
Cyclic voltammetry

ABSTRACT

Nb-94, an activation product in irradiated cladding, is a major concern in geological disposal. As Nb-94 is distributed throughout the cladding, volumetric decontamination should be applied for separation between Zr and Nb. In this study, the radiological characteristics of irradiated HANA-4 cladding were investigated using the ORIGEN-ARP code to derive a decontamination factor for Nb-94, 11. The electrochemical behavior of Nb was evaluated by cyclic voltammetry using low $NbCl_5$ concentrations (0.15 and 0.5 wt %) in LiCl-KCl at 773 K. Nb exhibits complex redox behaviors, but it was found that the nobler tendency could be utilized for Zr electrorefining. Two electrorefining tests were performed by applying constant potentials of −0.85 V and −1.2 V (vs. Ag/AgCl 1 wt %) at the anode and cathode, respectively. From the anodic test, Zr metal was obtained at the bottom of the salt, by two-step reactions among Zr^{4+}, Zr^{2+}, and Zr. Meanwhile, ZrCl and Zr were co-recovered as deposits in the cathodic test. The results revealed good separation performance between Zr and Nb. The Nb concentrations were 2.1 and 20.3 ppm in the products from the anodic and cathodic tests, respectively, supporting the feasibility of satisfying the radioactivity concentration limits of the Gyeongju Disposal Facility.

1. Introduction

Zr is widely utilized in different types of nuclear power plants because of its low thermal neutron capture cross-section and high hardness [1,2]. Generally, Nb is added to Zr alloys, such as ZIRLO and HANA claddings, to increase their corrosion resistance [3,4]. These alloys are commercially used as fuel claddings in PWRs. The fuel claddings are then exposed to a high neutron flux and, as a result, activation products are easily located within the components. A stable isotope of Nb can generate Nb-94 via neutron activation under a high neutron flux during the operation of nuclear reactors [1]. According to an assessment of the radioactive characteristics of different types of nuclear fuel claddings, Nb-94 is among the most important contributors to increases in radioactivity in irradiated claddings [5]. This indicates that spent fuel cladding cannot satisfy the radioactivity concentration limit of Nb-94 for the geological disposal of low- and intermediate-level waste at Gyeongju Disposal Facility, Republic of Korea [6].

Unlike contaminating radionuclides, activation products are uniformly distributed throughout the waste volume. This indicates that surface decontamination is not effective, and volumetric decontamination should be considered to reduce both the volume of radioactive waste and the waste level of spent nuclear fuel cladding. Furthermore, cladding hulls occupy approximately 40% of the volume of spent nuclear fuel, which causes the continuous accumulation of radioactive waste. Electrorefining would be a promising solution to this problem, as it can decontaminate metallic radioactive waste by dissolving the entire waste volume at the anode and selectively recovering major alloying elements at the cathode based on the difference in Gibbs free energy of formation. The radioactivity concentration limit for Nb-94 at Gyeongju Disposal Facility increased from 110 to 149,000 Bq/g in July 2024, enabling the geological disposal of irradiated Zr-Nb alloy claddings by volumetric decontamination via electrorefining.

Electrochemical studies have been widely conducted to separate Zr-Nb alloys by using molten salt electrolytes at high temperatures. Numerous studies have employed cyclic voltammetry (CV) to evaluate the electrochemistry of Zr in chlorides with different conditions, such as

* Corresponding author.
E-mail address: jypark@unist.ac.kr (J. Park).

https://doi.org/10.1016/j.net.2026.104252
Received 20 October 2025; Received in revised form 15 January 2026; Accepted 6 March 2026
Available online 7 March 2026

temperature, $ZrCl_4$ concentration, and working electrodes [7–14]. Although many studies have investigated the electrochemical behavior of Nb, specific experimental conditions still have to be assessed regarding determination of molten salt electrolyte [15–21].

The fluoride systems promote dendritic Zr growth due to simple Zr electrochemistry which leads to advantages in cathode processing, but cause corrosion issues on structural materials. The chloride systems have a lower melting point and less corrosivity than the fluoride system, but powdery Zr and ZrCl would be recovered due to the complicated disproportionation reaction of Zr. Previous electrorefining results of Zr alloys in the presence of fluorides showed coarse Zr metal recovered at cathode [22–24]. Fujita et al. conducted electrorefining of BWR channel box material in a LiCl-KCl-LiF at 650 °C under anodic current control and obtained 99.9 % pure Zr with decontamination factor (DF) of approximately 400 for Co-60 [22]. Park et al. conducted electrorefining of Zirlo scrap in LiF-KF at 700 °C and achieved pure Zr with less than 30 ppm of Nb [23]. Lee et al. examined electrorefining of Zirlo in LiCl-KCl-LiF at 600 °C and demonstrated that Zr metal could be recovered at −1.0–-1.1 V depending on the electrolyte composition [24]. On the other hand, chloride systems revealed co-deposition of fine Zr and ZrCl despite suppression of impurities at cathode [25–28]. Lee et al. investigated Zircaloy-4 electrorefining in LiCl-KCl at 500 °C and reported that Zr or ZrCl is deposited at cathodic potentials of −1.15 V and −1.55 V, respectively [25]. Sohn et al. reported Zircaloy-4 electrorefining in LiCl-KCl at 500 °C under anodic control at −0.9 V and showed chemical form of deposit change from Zr to ZrCl depending on the initial $ZrCl_4$ concentration [26]. Hur et al. showed Zr-2.5Nb in LiCl-KCl at 500 °C and presented low concentration of Nb at cathode at the early stage of electrorefining [27]. Finally, Hur et al. examined Zr-2.5Nb electrorefining in LiCl-KCl at 450 °C and reported cathodic formation of ZrCl at −1.1 V and subsequent conversion from ZrCl to Zr metal by thermal decomposition [28]. However, further investigations for electrorefining of Zr-Nb alloys in chloride-based systems which allow operation at lower temperatures and exhibit better compatibility with structural materials are required for potential engineering applications.

To investigate the feasibility of the electrolytic process as a volumetric decontamination method, this study assessed the recovery of Zr from irradiated HANA-4 scrap via electrorefining in chloride salts. Before conducting electrochemical experiments, ORIGEN-ARP calculations were performed to derive the decontamination target and the separation goal by analyzing the radiological characteristics of the irradiated HANA-4 in PWRs. The electrochemical behavior of Nb in molten LiCl-KCl salts at 773 K was investigated via CV using $NbCl_5$ (0.15 and 0.5 wt %) to determine the operating conditions for electrorefining. Potentiostatic electrorefining tests were then performed using a potential control to suppress Nb deposition at the cathode. Fresh HANA-4, as well as Co and Ni wires, were used as anode materials to simulate the irradiated structure. The elemental composition and chemical formulas of the recovered Zr products were analyzed to evaluate the efficiency of the process.

2. Radiological characteristics of HANA-4

Assuming representative operating conditions for domestic PWRs, the radiological characteristics of the HANA-4 alloy during irradiation, and the post-irradiation period were evaluated using the ORIGEN-ARP code [29]. The reference case considered was a domestically standardized PLUS7 16 × 16 fuel assembly operated under a three-batch fuel management scheme with an average discharge burnup of 55 GWD/tU. The evolution of nuclide-specific radioactivity in HANA-4 was subsequently calculated as a function of time. The elemental composition of HANA-4 [2] is listed in Table 1.

The calculation results indicated that Nb-94 ($T_{1/2}$ = 20,400 years) was the primary contributor to the radiological source term of HANA-4 over a cooling period of less than 1000 years (Fig. 1). Although other long-lived radionuclides, such as Ni-59 ($T_{1/2}$ = 80,000 years), Ni-63 ($T_{1/2}$ = 100 years), and Tc-99 ($T_{1/2}$ = 211,000 years), were present, their initial activities were approximately five orders of magnitude lower than that of Nb-94. Co-60 ($T_{1/2}$ = 5.27 years) exhibits a significant contribution to the total activity in the early stage after discharge, following Nb-94, but decays rapidly owing to its short half-life. Consequently, Nb-94 remained the dominant nuclide of radiological concern at the assumed disposal time, which was equivalent to a cooling time of 40 years after discharge from the reactor. This was attributed to the fact that Nb was the major alloying constituent of HANA-4.

Table 1
Composition of fresh HANA-4 alloy (wt. %) [4].

	Nb	Sn	Fe	Cr	Zr
HANA-4	1.5	0.4	0.2	0.1	Bal.

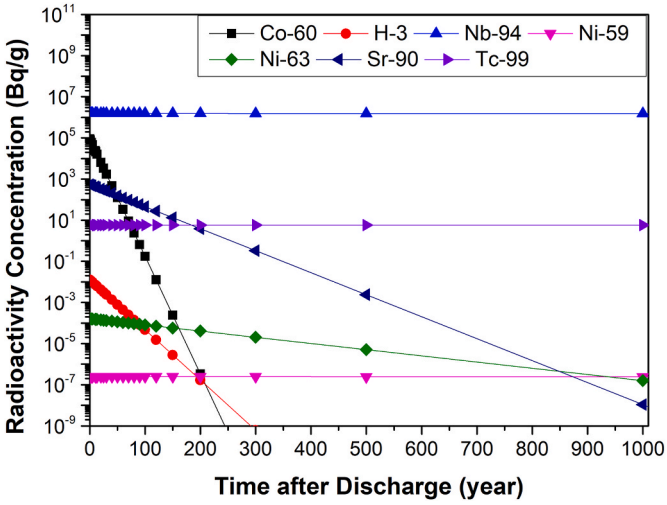

Fig. 1. Radioactivity concentration changes of major radioisotopes in irradiated HANA-4 cladding after discharge burnup of 55 GWD/tU in PWR calculated by ORIGEN-ARP.

For the final disposal of HANA-4 cladding separated from spent nuclear fuel, the concentrations of all relevant radionuclides at the time of disposal must satisfy the nuclide-specific acceptance criteria stipulated for the currently operating low- and intermediate-level waste repositories in Gyeongju [6]. All radionuclides satisfied the radioactivity concentration limit indicated in the waste acceptance criteria of the safety analysis report, except for Nb-94, for which the concentration exceeded the limit by approximately 11 times. This indicates that the separation of Nb-94 from irradiated HANA-4 cladding scrap is crucial for satisfying the waste acceptance criteria in terms of the radioactivity concentration limit before disposal. In addition, the use of electrolytic separation processes to achieve the decontamination factor goal is feasible.

3. Experimental

Because employing molten chloride salts at 773 K requires an inert atmosphere, CV and electrorefining were performed within a glove box filled with Ar gas of 99.999% purity. The oxygen and moisture contents were maintained below 0.1 ppm. Electrochemical cells were placed inside a Type 304 stainless-steel furnace surrounded by a jacket heater. A PAR Versastat3 potentiostat, controlled using the Versastudio software, was used to apply and measure electrochemical signals. In the CV and electrorefining experiments, Ag/AgCl (1 wt %), composed of a Pyrex membrane tube, an Ag wire (Sigma Aldrich, 99.99%, 1-mm diameter), LiCl-KCl eutectic salt (Sigma Aldrich, 99.99%), and AgCl (Sigma Aldrich, 99.999%), was used as the reference electrode. Hence, all

potentials described in this article are related to the Ag/AgCl 1-wt. % reference electrode.

3.1. CV

The target concentration of $NbCl_5$ was prepared using a two-step process because some $NbCl_5$ could be evaporated and lost during the preparation of LiCl-KCl-$NbCl_5$, owing to the lower melting point of $NbCl_5$ (521 K) relative to that of LiCl-KCl (625 K). Anhydrous $NbCl_5$ (Alfa Aesar, 99.95%) powder was loaded at the bottom of a quartz cell, after which LiCl-KCl beads were loaded into the cell. The salt-containing cell was placed in a furnace preheated to 873 K to rapidly increase the cell temperature above the melting point of LiCl-KCl. The content of $NbCl_5$ was identified as 6.05 wt % via inductively coupled plasma–optical emission spectroscopy (ICP-OES) and ICP–mass spectroscopy (ICP-MS). The salts were diluted using LiCl-KCl to the target concentration of $NbCl_5$ for the CV experiment.

The electrochemical cells were arranged in a quartz tube with an inner diameter of 13 mm and height of 380 mm. Tungsten wires (Sigma Aldrich, 99.99%, 1-mm diameter) were used as the working and counter electrodes. Diluted salt (3.0 g) with different concentrations of $NbCl_5$ was loaded into the quartz tube, and the temperature increased to 773 K. The surface area of the reactive electrode was estimated as 0.628 cm^2 by measuring the immersion depth of the tungsten wire.

According to previous studies, Nb exhibits highly complex electrochemical behavior in halide electrolytes at high temperatures [15–21]. Although the overall tendencies appear similar, some inconsistencies exist in the literature, which can be attributed to the temperature, the charge valence of Nb ions depending on the Nb precursor (e.g., $NbCl_5$ and Nb_3Cl_8), the Nb concentration in the electrolyte, and the effect of additional anions present in the electrolyte. To separate Zr and Nb from a mixture, it is important to understand the dependence of the Nb redox behavior on the concentration of $NbCl_5$ in the electrolyte, as Nb might be dissolved during the electrorefining of irradiated HANA-4. Therefore, the electrochemical redox behavior of Nb was investigated at relatively low concentrations (e.g., 0.15 and 0.5 wt %). In addition, CV measurements were performed in an environment in which $ZrCl_4$ (1 wt %) and $NbCl_5$ (0.1 wt %) coexisted in LiCl-KCl at 773 K, to observe the electrochemical behavior under conditions similar to those of actual salts during electrorefining.

The redox behavior of Zr is much more complex than that of Nb. Numerous related studies have been performed at different Zr^{4+} concentrations, and similar trends have been identified [7–14]. Co^{2+} and Ni^{2+} showed simple redox characteristics in high-temperature LiCl-KCl, and it has been determined that these noble elements do not affect the performance of electrorefining [12,30–32]. Therefore, the CVs for Zr, Ni, and Co were not considered in this study.

3.2. Potentiostatic electrorefining of HANA-4 materials

As shown in Fig. 2, electrorefining experiments were performed at 773 K in a quartz tube (inner diameter, 27 mm; height, 380 mm) containing LiCl-KCl and 5-wt. % $ZrCl_4$ (Sigma Aldrich, 99.99%). A tungsten rod (Alfa Aesar, 99.95%, 3.175-mm diameter) was used as the cathode since it is widely known as an inert electrode material for molten salt application. The tungsten rod was threaded to diminish deposit detachment during electrorefining, as shown in Fig. 3(a). The anode material, HANA-4 scrap (inner diameter, 8.37 mm; outer diameter, 9.5 mm; height, 40 mm), was provided by KEPCO Nuclear Fuel CO., Ltd. The anode was prepared by loading a cylindrical HANA-4 specimen into a Type 316 stainless-steel basket (diameter, 10 mm; height, 25 mm), as shown in Fig. 3(b). In addition, small amounts of Co (99.995%, 1-mm diameter) and Ni (99.995%, 1-mm diameter) wires were added to the basket to simulate the activation products.

Two electrorefining tests were conducted using a potentiostatic method. Run 1 was conducted by applying −0.85 V at the anode basket

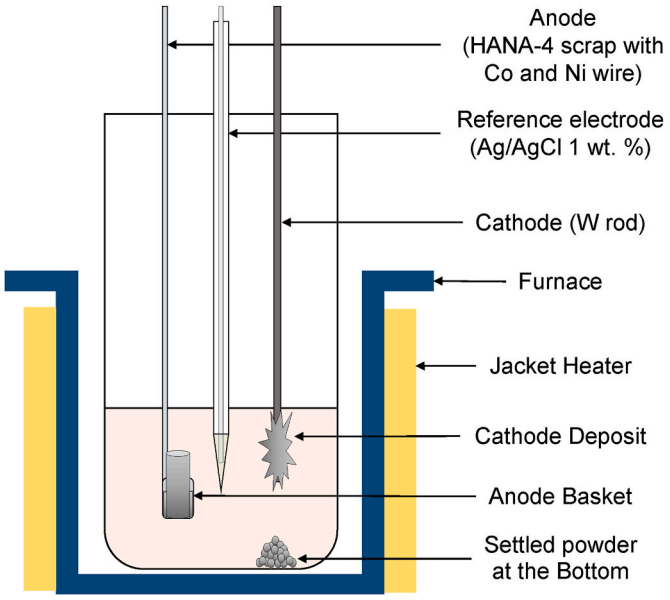

Fig. 2. Schematic configuration of electrorefining cell.

to dissolve Zr from the HANA-4 and to leave Nb at the anode basket and induce the reduction reaction of Zr^{4+} to Zr^{2+} at the cathode. Run 2 was conducted by applying a cathode potential of −1.2 V to selectively recover Zr products at the cathode rod and to evaluate the behavior of Nb under conditions that covered nearly the full anodic dissolution, as the applied charge approached the theoretical dissolution limit of the anode. The reduction of ZrCl, an insoluble intermediate product, can result in the formation of Zr metal at −1.15 V [10]. Both the anodic and cathodic potential-controlled experiments were conducted for 10 h to obtain sufficient deposits. The crystallographic characteristics and chemical forms of the cathode deposits and powders observed at the bottom of the cell were determined using X-ray diffraction (XRD). Meanwhile, the elemental compositions of the deposits and molten salts were analyzed via ICP-OES and ICP-MS.

4. Results and discussion

4.1. CV

Fig. 4 shows two cyclic voltammograms for $NbCl_5$ (0.15 wt % and 0.5 wt %) in LiCl-KCl salts, obtained at 773 K. Regardless of the scan rate and concentration of $NbCl_5$, complex electrochemical behavior was observed owing to the different reduction and oxidation states of Nb ions. Both results showed highly analogous shapes and potentials for the three reduction peaks and four oxidation peaks. In a previous study investigating the redox behavior of Nb, which was measured at 723 K via CV, for 1.0-wt. % $NbCl_5$ in LiCl-KCl, four reduction and five oxidation peaks were found in the voltammogram [21]. Although the temperatures and concentrations differed, the overall peak shapes were in good agreement with those of the reference case. However, a redox pair attributed to Nb subchlorides ($NbCl_x$) did not appear in the voltammogram at either $NbCl_5$ concentration. Specific redox reactions were observed at each peak in the voltammograms.

As the potential scan proceeded from 1.0 V in the negative direction, the reduction of Nb^{5+} and Nb^{4+} occurred at R1 and R2, respectively, and Nb^{3+} was formed. At the R3 peak, Nb metal deposition occurred through the reduction of trivalent ions, resulting in the largest peak current in the voltammogram. As the potential scan proceeded in the positive direction, the oxidation of the Nb metal deposited on the working electrode occurred at O1. Another oxidation peak, O2, emerged at the shoulder of O1. These oxidation peaks may be related to the oxidation of Nb metal to

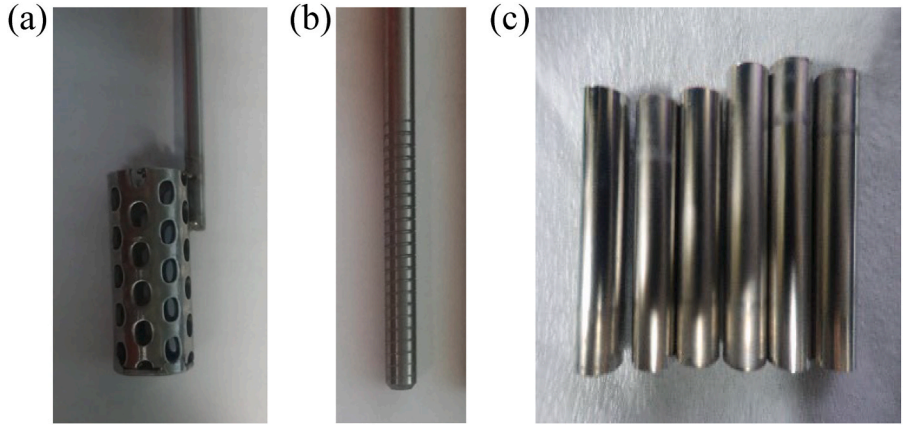

Fig. 3. Optical images of (a) tungsten cathode, (b) anode basket, and (c) HANA-4 scrap specimens.

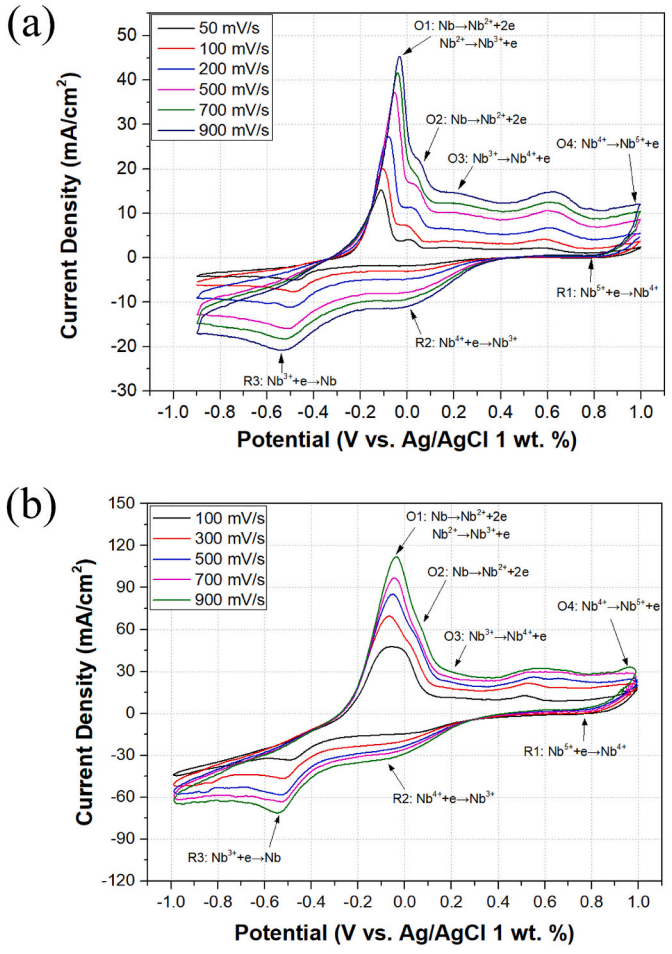

Fig. 4. Cyclic voltammogram of (a) $NbCl_5$ (0.15 wt %) and (b) $NbCl_5$ (0.5 wt %) in LiCl-KCl at 773 K.

various ion valences of Nb [18,19,21]. Following the formation of peak O2, peak O3 immediately emerged as an oxidation peak corresponding to R2. Subsequently, the final oxidation reaction of tetravalent ions to pentavalent ions occurred, at approximately +1.0 V.

Regarding peak O2, the peak current was much smaller than that of O1 for 0.15-wt. % $NbCl_5$, as shown in Fig. 4(a). However, for 0.5-wt. % $NbCl_5$, the height of peak O2 increased significantly and tended to merge with O1 (Fig. 4(b)). This tendency is consistent with the results obtained from studies that used 1-wt. % $NbCl_5$. Based on these characteristics, it was inferred that the oxidation peak of Nb^{3+}/Nb^{4+} tended to increase when the $NbCl_5$ concentration exceeded a certain level (e.g., 0.6 wt %).

The main reduction peak in the $NbCl_5$ voltammogram, related to ion/metal reactions, occurred at approximately −0.55 V. A comparison of the CV results of Nb with those of Zr measured in LiCl-KCl-$ZrCl_4$ at 773 K, as shown in the literature, revealed a large potential difference between Zr and Nb found at both the anodic and cathodic sides [10,12,21].

Fig. 5 shows a cyclic voltammogram for $ZrCl_4$ (1.0 wt %) and $NbCl_5$ (0.1 wt %) coexisting in LiCl-KCl at 773 K. The two main reduction peaks of Zr, one located at Zr^{4+}/ZrCl (R2) and the other at ZrCl/Zr (R3), were observed at approximately −1.15 V and −1.5 V, respectively. The main oxidation peak, O1, corresponded to the Zr/Zr^{4+} reaction, while the broad shoulder on the right side of O1 was attributed to the Zr^{2+}/Zr^{4+} reaction. These peak behaviors are in good agreement with those of previous studies [10,12]. In addition, disproportionation reactions of Zr were clearly observed, despite the coexistence of multiple elements in the molten salt electrolyte.

As the concentration of Nb was much lower than that of Zr, a slight peak attributable to Nb was observed as R1 and O3. Although the Nb precursor was a pentavalent ion, other peaks formed via the reactions identified from the CV for $NbCl_5$ could not be distinguished owing to the low concentration. The potential difference between R1 and R4, that is, the reduction peaks related to the formation of Zr and Nb metals, was approximately 0.9 V, consistent with the separation observed in the

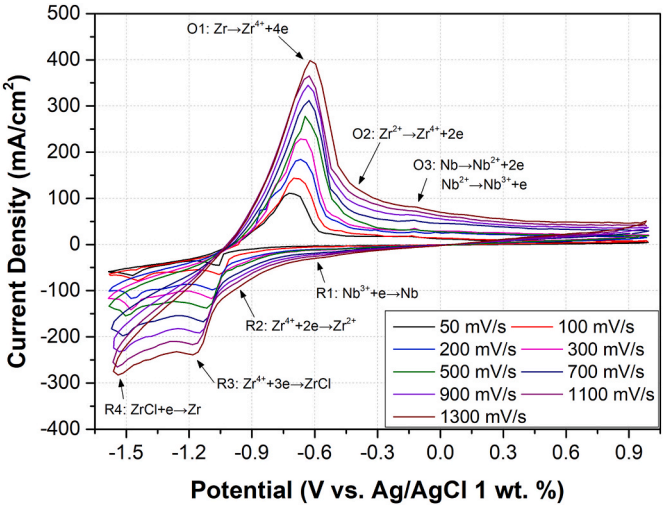

Fig. 5. Cyclic voltammogram of $ZrCl_4$ (1.0 wt %) and $NbCl_5$ (0.1 wt %) in LiCl-KCl at 773 K.

individual CVs. Moreover, the difference between R1 and R2 was 0.4V, suggesting that the electrolytic separation of Zr and Nb could be achieved by controlling either the anode or cathode potentials. Applying a more negative potential to the cathode could lead to better Zr metal reduction, but a large overpotential causes the dissolution of Nb from the anode and a decrease in current efficiency. Therefore, the applied cathode potential was determined to be −1.2 V for selectively reducing Zr without Nb onto the cathode rod during run 2. Meanwhile, in run 1, the anode potential was controlled at −0.85 V, selectively oxidizing Zr from HANA-4 and inducing R2 reaction at cathode rather than R3 to obtain Zr metal by disproportionation reaction directly.

4.2. Anode potentiostatic electrorefining

Fig. 6(a) shows the potential and current changes during anodic potential-controlled electrorefining. The anode equilibrium potential was maintained at the intended value for 15 h. The transient potential deviation was less than 20 mV, which is not large enough to cause the dissolution of other HANA-4 alloying elements, except for Zr, and to aggravate the electrorefining performance. The current also remained constant at approximately 200 mA, indicating that insoluble deposits (e.g., Zr metal and ZrCl) that can enlarge the cathode surface area were unlikely to be formed. Fig. 6(b) shows that no deposits were found on the cathode after anodic potential-controlled electrorefining. The transferred charge can be used to reduce Zr^{4+} to another soluble ion, Zr^{2+}, at the cathode surface, as shown in Eq. (1). The reaction generally started at approximately −0.8 V, more positive than the potential for ZrCl formation of approximately −1.1 V [10,12].

$$Zr^{4+} + 2e^{-} \rightarrow Zr^{2+} \quad (1)$$

Although no deposits were produced on the cathode, considerable amounts of black powder were found at the bottom of the salts (Fig. 7(a)). The powder scraped from the bottom of the salt ingot was identified by XRD as Zr metal (Fig. 7(b)). The other peaks not marked in the XRD pattern corresponded to LiCl-KCl-$ZrCl_4$ [26]. Since the electrochemical formation of Zr metal from Zr^{4+} occurs at a much more reductive potential of at least −1.2 V where ZrCl is produced, the precipitated powder would not result from a cathodic reaction but from a disproportionation reaction of Zr^{2+} and the white-to-brown color of salt ingot supports that the Zr^{2+} in the salt was consumed by reaction (2) as follows [8,13,24]:

$$2Zr^{2+} \leftrightarrow Zr + Zr^{4+} \quad (2)$$

Since no evidence of ZrCl was found at the cathode during the anode potentiostatic electrorefining, it is confirmed that the soluble/soluble reduction reaction occurred at the cathode with a more positive potential than that of ZrCl deposition. The estimation of Zr^{2+} formation as the soluble product at the cathode was inferred by comparison with our previous work and other earlier studies [8–10,25]. However, Cha and Yun suggested that the first reduction step of Zr^{4+} at the most positive potential corresponds to the Zr^{4+}/Zr^{3+} reaction, and consequently, metallic Zr could be formed during the electrorefining as following reaction (4) [13]:

$$Zr^{4+} \rightarrow Zr^{3+} + e \quad (3)$$

$$4Zr^{3+} \leftrightarrow Zr + 3Zr^{4+} \quad (4)$$

As electrorefining progressed under a low cathodic current density, Zr^{2+} gradually accumulated in the molten salt according to reaction (1) and was disproportionated into Zr metal and Zr^{4+} when Zr^{2+} was supersaturated. The Nb content in the metal precipitate collected at the lower part of the used salt was identified by ICP-MS as 2.1 ppm. This concentration is equivalent to a DF of 7100 compared with the Nb concentration in initial HANA-4 material. No other alloying elements were detected, indicating that the anode potential was appropriately controlled to prevent unnecessary elemental dissolution. Therefore, highly decontaminated Zr metal can be obtained by retrieving black powder precipitates.

The electrochemical equilibrium between the Nb at the anode and the salts explains the Nb content of the salts used. It has been reported that the dissolution of Nb metal occurs with a formal potential ranging from −0.31 to −0.37 V, depending on the experimental methods and related Nb ions [21]. When the Nb content in the salts was 1 ppm, the equilibrium potential between Nb metal and Nb ions was −0.78–-0.84 V which is close to the anode potential applied in this study, approximately −0.855 V. The dissolved Nb could be reduced to metal and detached at cathode, and precipitated with the Zr deposits. Considering that the dissolved Nb ion is preferentially deposited as metal phase at the cathode, the analyzed Nb concentration in the metal precipitate at the salt bottom indicates that Nb is rarely dissolved at the anode, corresponding to both the CV results and the anode equilibrium potential transient during the electrorefining in this study. In a previous study on Zircaloy-4 electrorefining, the anodic potential was maintained at −0.9 V for various $ZrCl_4$ contents (0.1, 0.5, 1, 2, and 4 wt %). The resulting insoluble cathode deposits consisted of ZrCl, Zr metal, or a mixture of both [26]. Even at a more negative anode potential, the formation of insoluble deposits is due to the larger surface area ratio of the anode relative to that of the cathode. A previous study found that the reactive anode area was approximately five times larger than that of the cathode; Zircaloy-4 specimens were cut into six small pieces and loaded into an anode basket, and the diameter of the tungsten rod used was 3.175 mm. However, in this study, the active area of the anode was less than three times, approximately 2.98, that of the cathode; a cylindrical HANA-4 specimen with a diameter of 9.5 mm was loaded in the basket without chopping, and a threaded tungsten rod with a diameter of 3.175 mm was used. Assuming that the outer surface area of the HANA-4 specimen

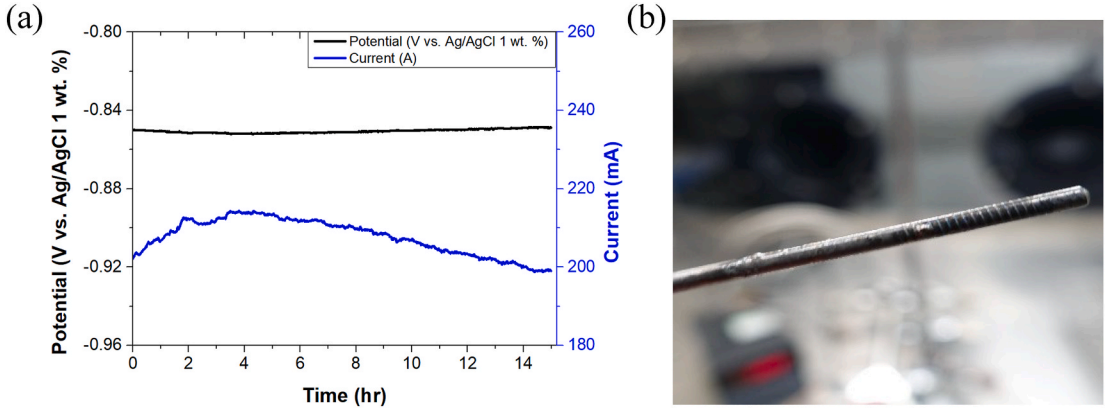

Fig. 6. (a) Anode potential and current during the anode potentiostatic electrorefining and (b) optical image of the W rod as cathode after the electrorefining.

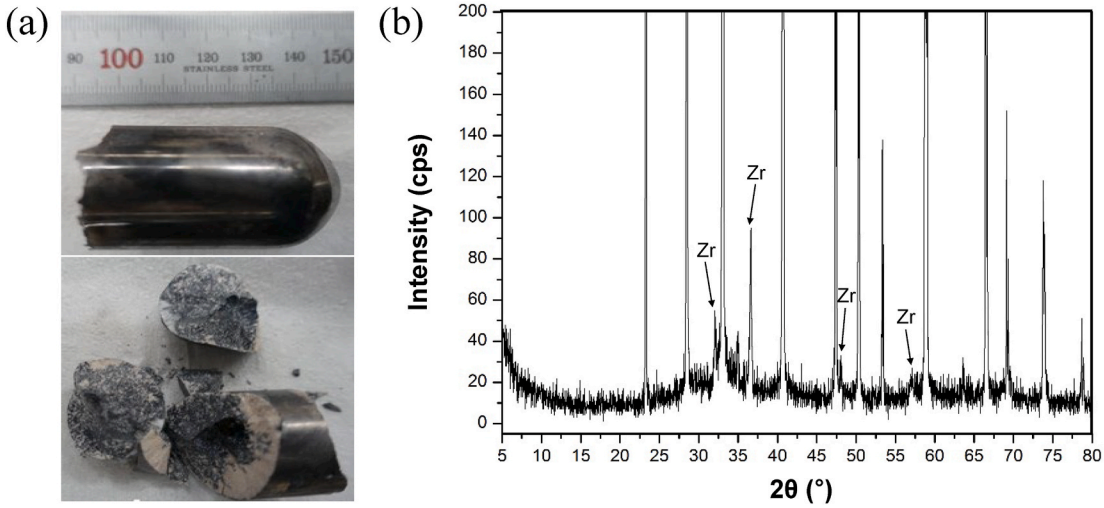

Fig. 7. (a) Optical images and (b) XRD patterns of the black powder precipitates accumulated at the bottom of the electrolyte salts after the anode potentiostatic electrorefining (All peaks found except the Zr peaks are related to LiCl-KCl-$ZrCl_4$).

which was overlapped with the anode basket had a disadvantage in terms of mass transfer, the effective anode surface area was defined by the summation of the outer surface area directly exposed to molten salt and inner surface area, calculated to be 15.14 cm^2. The cathode surface area was determined by the immersed height in the molten salt, calculated to be 5.09 cm^2. When the anode to cathode ratio was approximately 5 in the previous study, the cathodic current density was sufficient to reach the cathode potential beyond −1.2 V, favoring the ZrCl formation and subsequently Zr metal. In contrast, when the surface area ratio was reduced to 2.98 in this study, the cathodic current density decreased and the cathode potential was maintained below −1.0 V, where the reduction of Zr^{4+} to Zr^{2+} is dominant and the further deposition of ZrCl could not proceed. If ZrCl is deposited at cathode, additional electron consumption is required to form Zr metal. In contrast, formation of Zr^{2+} leads to Zr metal formation without electron consumption as represented in reaction (2). Therefore, the current efficiency would be enhanced by employing smaller anode-to-cathode area ratio.

Assuming that the anodic current efficiency is 100%, that no side reactions such as chlorine evolution and anode basket corrosion occurred, the passed charge of 11,200 C for 15 h is equivalent to dissolving 63.6% of the anode material. This estimation is considered reasonable since the anode equilibrium potential remained stable to oxidize Zr. Also, Zr composition in the anode material is approximately 98%, and oxidation of other alloying elements was almost suppressed, which can be determined by the stable anode potential. In other words, the entire electrorefining process was considered as a period in which Zr continues to be oxidized at the anode. Although the present electrorefining test did not proceed to the point where the anode material is completely consumed, these results demonstrate the possibility of anodic potential control to sustain the electrorefining process with Zr metal production beyond the intermediate stage. Hur et al. reported anode potentiostatic electrorefining of Zr-2.5Nb alloy in the chloride system, but they revealed the Nb suppression in the early stage of electrorefining, equivalent to the point at which approximately 18% of Zr-2.5Nb was dissolved.

Although the weight of the residual anode material and the zirconium metal collected from the bottom of the molten salt were not quantified, the fact that the anodic potential and the corresponding current remained stable for 15 h, together with the absence of any visible cathodic deposition, suggests that the refining process proceeded stably without significant electron consumption in undesirable side reactions both at the anode and the cathode. This inference is reasonable because the only competitive anodic reactions are the dissolution of the anode basket and chlorine evolution, and the only competitive cathodic reaction is the deposition of ZrCl. In addition, the applied anodic potential of −0.85 V was sufficiently negative to suppress oxidation of both the alloying elements in HANA-4 and the SS304 basket, and no evidence of ZrCl was observed at both the cathode and at the bottom of the melt.

4.3. Cathode potentiostatic electrorefining

Fig. 8 presents the cathode potential and current during electrorefining, where we aimed to maintain the cathode potential at −1.2 V. The actual cathode potential gradually increased from −1.17 to −1.05 V, and the current also changed following the potential transition. The prolonged transition in current and potential observed during electrorefining was presumed to originate from dynamic changes in the effective electrode surface area, associated with anodic dissolution and cathodic deposition, along with the time-dependent relaxation of the concentration gradients toward steady-state equilibrium. This behavior is similar to that observed in a previous study conducted at KAERI [25].

As electrorefining progressed, solid deposits were obtained at the cathode, as shown in Fig. 9(a). Excluding the molten salt attached to the cathode, the deposited products were identified via XRD analysis as ZrO_2, Zr, and ZrCl (Fig. 9(b)). Although the main peaks of ZrO_2 and KCl overlapped in the XRD pattern, ZrO_2 could be distinguished from the other peaks. Considering that the Zr peaks were clearly distinct in the

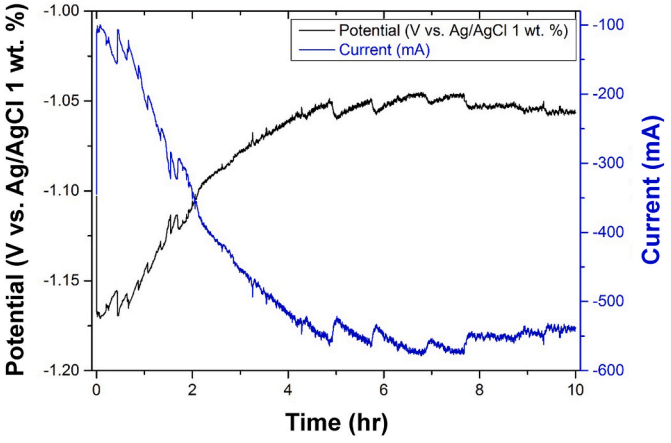

Fig. 8. Cathode potential and current during the cathode potentiostatic electrorefining.

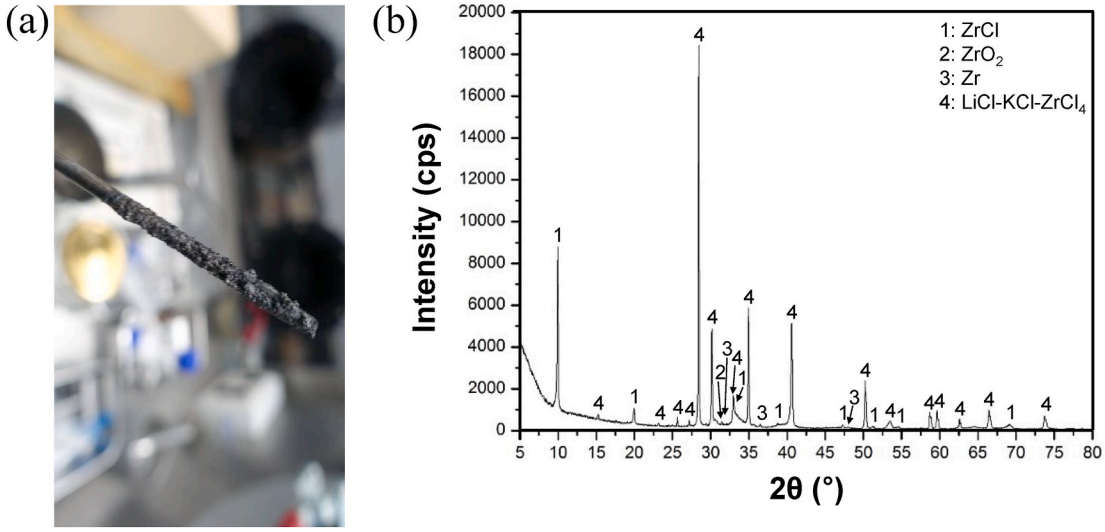

Fig. 9. (a) Optical image and (b) XRD pattern of electrodeposits recovered at the cathode after cathode potentiostatic electrorefining.

analysis results of the precipitates from anode potentiostatic electrorefining shown in Fig. 7(b), ZrO_2 was formed by the oxidation of Zr during the analysis outside the Ar environment. Therefore, the Zr compounds deposited at the cathode were Zr and ZrCl. According to the literature, Zr^{4+} can be reduced to ZrCl in LiCl-KCl at approximately −1.10 V, as follows [8,12,25]:

$$Zr^{4+} + 3e + Cl^{-} = ZrCl \quad (5)$$

Although the cathodic current increased from the starting point to the middle stage of the electrorefining, only a small amount of Zr compounds were observed at the cathode deposit. It could be attributed to detachment of ZrCl from the cathode. As a result, a considerable amount of ZrCl settled at the bottom of the molten salt as shown in Fig. 10(a). Considering that the cathodic current remained high within 5–10 h, the latter part of the electrorefining, it is estimated that the detachment would occur after the electrorefining due to unexpected and unidentified disturbance. This indicates that the threaded cathode is not effective to prevent the detachment of fine powders and an effective cathode design is required for cathode product recovery.

The XRD pattern in Fig. 9(b) shows a much stronger intensity for the ZrCl phase than for the other deposited phases, indicating that ZrCl was the predominant reduced species at the cathode. This is consistent with CV and other electrorefining results [10,12,13,25–28].

Fig. 10(a) shows the precipitates that settled at the bottom of the molten salt. Moreover, the XRD analysis results shown in Fig. 10(b) reveal that the main phase collected at the bottom of the salt was ZrCl, accompanied by some ZrO_2 and metallic Zr. The presence of ZrO_2 was considered to result from oxidation during the analysis outside the Ar atmosphere. The identification of Zr in the cathode deposit and at the bottom of the molten salt can be explained by the disproportionation reactions of Zr, as shown in reactions (1) and (2). Consistent with the morphology of the cathodic deposits and the XRD results in Fig. 9, a significant portion of the ZrCl deposit detached from the cathode and accumulated at the bottom of the molten salt (Fig. 10).

The passed charge during the electrorefining was calculated to be 16,000 C based on the current transient, which is equivalent to dissolving 90.8% of the anode materials with the anode current efficiency being 100%. Therefore, it is regarded that the electrorefining progressed to a late stage of anode dissolution. From the current-potential transient curve, ZrCl deposition was dominant during the early stage, and co-deposition of ZrCl and soluble Zr species may have occurred later as cathode equilibrium potential was shifted positively. Unlike the anodic control case, a weak signal from Zr metal in the XRD pattern indicates that most of Zr^{2+} participated not in the reaction (2) to form Zr metal but in the ZrCl formation reaction (Zr^{2+}/ZrCl) with electrons at the cathode.

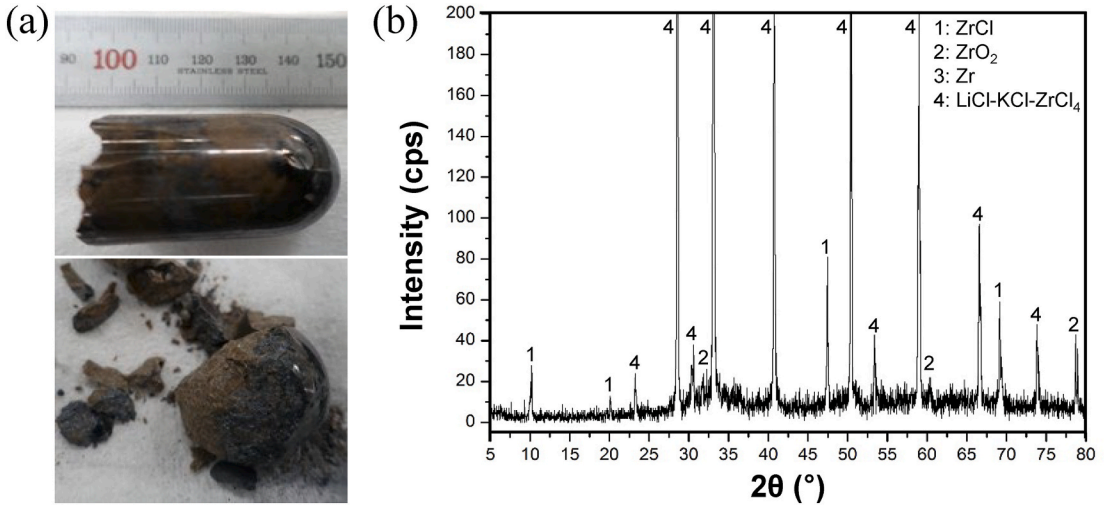

Fig. 10. (a) Optical image and (b) XRD pattern of precipitates accumulated at the bottom of electrolyte salts after the cathode potentiostatic electrorefining.

Therefore, the cathodic current efficiency would be significantly lower under cathodic potential control since ZrCl formation from the Zr^{4+} or Zr^{2+} requires more electron than the Zr metal formation by reaction (2).

The concentration of Nb in the ZrCl deposits collected at the cathode and salt bottom was found to be 20.3 ppm. This concentration is equivalent to a DF of 730. K. Park et al. reported that the DF of Nb is estimated to be more than 330 in the Zirlo scrap electrorefining using fluoride [23]. This could be attributed to larger-scale experiments than those in this study.

The concentrations of Co and Ni were found to be below the ICP-MS detection limit, suggesting no dissolution from the anode. The purity of Zr in the cathode deposits was estimated to be 99.94%. Therefore, it was shown that electrorefining can be a feasible option for the geological disposal of irradiated Zr-Nb alloys in the Republic of Korea.

Regarding the Nb distribution in the electrorefining system, Nb has a more positive reduction potential than Zr. Once Nb is dissolved from the anode, it should be electrodeposited at the cathode prior to Zr. In anode potentiostatic electrorefining, the undissolved Nb is considered to remain in the anode basket since Nb was not detected at the bottom of the salt. In cathode potentiostatic electrorefining, the Nb concentration in the collected ZrCl deposits at the cathode and the salt bottom was found to be 20.3 ppm and this is attributable not to the anode form but to oxidized and deposited form due to the absence of Co and Ni in the deposit. In addition, the concentration of Nb quantitatively analyzed by ICP-MS is equivalent to the amount of Nb dissolved at the anode and deposited to the cathode. Therefore, the low concentrations revealed that the Nb separation was effectively achieved by the anodic and cathodic potentiostatic methods.

4.4. Engineering considerations and conceptual recovery strategies for Zr and ZrCl powders in scaled-up systems

During electrorefining of HANA-4 cladding in LiCl–KCl molten salts, Zr solid products were generated under both anodic and cathodic potential-controlled conditions and were observed to accumulate at the bottom of the electrolyte. Although the chemical composition of these products varies depending on the electrochemical reaction, the post-processing methods in both cases are identically required to recover the fine particulates at the cell bottom using methods compatible with high-temperature molten salt systems.

Under anodic potentiostatic control, the recovered product consisted mainly of fine Zr metal powder formed via disproportionation reactions. In contrast, cathodic potentiostatic electrorefining resulted in a mixed powder composed mainly of ZrCl due to the reduction of Zr^{4+} to ZrCl and subsequent disproportionation. From the perspective of process integration, salt distillation would be the most favorable recovery method that can be applied to both Zr and ZrCl powder. Salt distillation has been widely employed in the pyroprocessing of used nuclear fuel to remove LiCl-KCl salts from cathode deposits. The boiling points of LiCl and KCl at atmospheric pressure are 1655 and 1420 K, respectively; therefore, the vacuum distillation of LiCl-KCl-based salts has been conducted at 1100–1400 K under 50–500 Pa, depending on the equipment design [33]. The salts generated in this study are expected to be treatable under similar operating conditions because the sublimation of $ZrCl_4$ occurs at 604 K [34]. In addition, it was reported that over 99.9% of salt could be recovered from the mixture of salt and rare earth metal powder as a result of salt distillation [28].

However, when it is applied to systems containing fine Zr powder, potential dispersion and loss of particles during salt distillation should be carefully considered. The Zr powder particles produced by the disproportionation reaction could be much smaller than the cathode deposits by hundreds of micrometers. In addition, the amount of salt mixed with the Zr metal powder was greater than the amount of deposit. Therefore, the evaporated salts could carry and scatter the fine Zr powder inside the distillation equipment. Analysis of the size distribution of the Zr black powder, as well as trial-and-error experiments on the equipment design, may be required to minimize the dispersion of Zr particles. Accordingly, recovery concepts may focus on equipment and operational designs that suppress entrainment of fine particles, such as controlled evaporation rates, internal flow barriers, and staged condensation, while promoting retention or consolidation of solid products within the distillation vessel. This strategy can be directly applied to anodic electrorefining in which the recovered product is mainly metallic Zr.

Meanwhile, the precipitated Zr black powder could be recovered via filtration through the lower part of the salt. The filtration equipment can be combined with a vacuum pump and a quartz filter with a pore size less than a micrometer, functional over the melting point of the salts (approximately 625 K). A high-power vacuum pump may not be necessary because of the fluidity of the molten salt, which was similar to that of aqueous solutions. Retrieving the Zr black powder from the filter would be challenging because the fine particles could remain stuck inside the filter and not be recovered via backwashing and scraping. This could result in the generation of secondary radioactive waste. The required and optimized specifications of the filter should be determined by analyzing the size distribution of the Zr black powder and using trial-and-error filtration tests.

In the case of cathodic potentiostatic electrorefining, where the settled ZrCl powders were observed, salt distillation can be coupled with a high-temperature thermal decomposition step under reduced pressure. Under vacuum conditions, ZrCl is converted into metallic Zr via thermal decomposition. This enables both the recovery of Zr in metallic form and the removal of residual salts. Previous studies demonstrated that ZrCl was decomposed at a specific temperature, but volatilization of $ZrCl_4$ may occur as an intermediate or a side reaction. Consequently, an effective recovery strategy should include a secondary condensation or collection system within the salt distillation apparatus, where temperature gradients are carefully controlled to condense and recover $ZrCl_4$ vapor for minimizing material loss and secondary waste generation [35].

5. Conclusions

This study achieved the volumetric decontamination of irradiated HANA-4 scrap via electrorefining to separate Zr and Nb. The ORIGEN-ARP results showed that Nb-94 was the primary contributor to the radioactivity concentration in irradiated HANA-4 after PWR operation, preventing the disposal of the irradiated alloy at Gyeongju Disposal Facility, Republic of Korea. The electrochemical redox behavior of Nb at low concentrations, similar to actual electrorefining conditions, was evaluated via CV. It was confirmed that this behavior was slightly simpler than that at high concentrations but consistent with the literature. In addition, CV revealed a sufficient potential difference between Zr and Nb when Zr and Nb coexisted in molten salt. Based on these results, two electrorefining tests were performed using anodic and cathodic potential controls, respectively. In anodic potentiostatic electrorefining, the anodic dissolution of Nb was suppressed. Meanwhile, Zr^{4+} dissolved at the anode was reduced to Zr^{2+} at the cathode, and Zr metal was formed in the molten salt electrolyte via Zr disproportionation reactions. In cathodic potentiostatic electrorefining, the inhibition of the cathodic electrodeposition of Nb was confirmed. Regarding the phase of the deposits, Zr^{4+} was reduced to ZrCl, and Zr metal was formed via disproportionation reactions between Zr^{4+}, Zr^{2+}, and Zr metal. The concentrations of Nb in the recovered product from anodic and cathodic potentiostatic electrorefining were found to be 2.1 ppm and 20.3 ppm, respectively, indicating that the radioactivity concentration limit of Gyeongju Disposal Facility was satisfied.

CRediT authorship contribution statement

Sungjune Sohn: Writing – review & editing, Writing – original draft, Project administration, Funding acquisition, Formal analysis, Data

curation, Investigation, Methodology. **Jungho Hur:** Writing – review & editing, Writing – original draft, Software. **Jaeyeong Park:** Writing – review & editing, Writing – original draft, Formal analysis, Data curation. **Pyeonghwa Kim:** Methodology, Investigation, Formal analysis. **Il Soon Hwang:** Supervision, Methodology, Conceptualization.

Conflict of interest

The authors declare that they have no known competing financial interests or personal relationships that could have appeared to influence the work reported in this paper.

Acknowledgements

This research was supported by the Korean Institute of Energy Technology Evaluation and Planning (KETEP) funded by the Ministry of Trade, Industry and Energy (MOTIE) (Grant RS-2023-00233988).

References

[1] Nuclear Data Center at Korea Atomic Energy Research Institute, Table of nuclides. http://atom.kaeri.re.kr:8080.
[2] E.R. Bradley, G.P. Sabol, Zirconium in the Nuclear Industry: Eleventh International Symposium, ASTM, West Conshohocken, Pennsylvania, 1996.
[3] ASTM B353-12, Standard specification for Wrought Zirconium and Zirconium alloy seamless and welded tubes for nuclear service, in: (Except Nuclear Fuel Cladding), ASTM, West Conshohocken, Pennsylvania, 2017.
[4] H.G. Kim, J.-Y. Park, Y.-H. Jeong, Y.-H. Koo, J.-S. Yoo, Y.-K. Mok, Y.-H. Kim, J.-M. Suh, IN-PILE performance of HANA cladding tested in Halden reactor, Nucl. Eng. Technol. 46 (2014) 423–430, https://doi.org/10.5516/NET.07.2013.093.
[5] M.K. Jeon, C.H. Lee, C.J. Park, J.H. Choi, I.H. Cho, K.H. Kang, H.-S. Park, G.I. Park, Effect of burn-up on the radio activation behavior of cladding hull materials studied using the ORIGEN-S code, J. Radioanal. Nucl. Chem. 298 (2013) 1629–1633, https://doi.org/10.1007/s10967-013-2543-6.
[6] Low and Intermediate Level Radioactive Waste Acceptance Criteria for Silo-type Radioactive Waste Disposal Facility. KORAD, WAC-SIL-2025-1, 2025.
[7] F. Basile, E. Chassaing, G. Lorthioir, Electrochemical reduction of ZrCl4 in molten NaCl, CsCl and KCl-LiCl and chemical reactions coupled to the electrodeposition of zirconium, J. Appl. Electrochem. 11 (1981) 645–651, https://doi.org/10.1007/BF00616685.
[8] Y. Sakamura, Zirconium behavior in molten LiCl-KCl eutectic, J. Electrochem. Soc. 151 (2004) C187–C193, https://doi.org/10.1149/1.1644605.
[9] S. Ghosh, S. Vandarkuzhali, P. Venkatesh, G. Seenivasan, T. Subramanian, B. P. Prabhakara Reddy, K. Nagarajan, Electrochemical studies on the redox behaviour of zirconium in molten LiCl-KCl eutectic, J. Electroanal. Chem. 627 (2009) 15–27, https://doi.org/10.1016/j.jelechem.2008.12.011.
[10] J. Park, S. Choi, S. Sohn, K.-R. Kim, I.S. Hwang, Cyclic voltammetry on zirconium redox reactions in LiCl-KCl-ZrCl4 at 500 °C for electrorefining contaminated Zircaloy-4 cladding, J. Electrochem. Soc. 161 (2014) H97–H104.
[11] R.O. Hoover, D. Yoon, S. Phongikaroon, Effects of temperature, concentration, and uranium chloride mixture on zirconium electrochemical studies in LiCl-KCl eutectic salt, J. Nucl. Mater. 476 (2016) 179–187, https://doi.org/10.1016/j.jnucmat.2016.04.037.
[12] J. Park, S. Choi, S. Sohn, I.S. Hwang, Cyclic voltammetry on Zr, Sn, Fe, Cr and Co in LiCl-KCl salts at 500°C for electrorefining of irradiated Zircaloy-4 cladding, J. Electrochem. Soc. 164 (2017) D744–D751, https://doi.org/10.1149/2.1501712jes.
[13] H.L. Cha, J.-I. Yun, Redox behaviors of zirconium in molten LiCl-KCl eutectic salt based on the comproportionation reaction between Zr(0) and Zr(IV), Electrochem. Commun. 84 (2017) 86–89, https://doi.org/10.1016/j.elecom.2017.10.010.
[14] W. Han, W. Wang, M. Li, J. Wang, Y. Sun, X. Yang, M. Zhang, Electrochemical behavior and extraction of zirconium on Sn-coated W electrode in LiCl-KCl melts, Sep. Purif. Technol. 232 (2020) 115965, https://doi.org/10.1016/j.seppur.2019.115965.
[15] F. Lantelme, Y. Berghoute, Transient electrochemical techniques for studying electrodeposition of niobium in fused NaCl-KCl, J. Electrochem. Soc. 141 (1994) 3306–3311, https://doi.org/10.1149/1.2059331.
[16] F. Lantelme, Y. Berghoute, A. Salmi, Cyclic voltammetry at a metallic electrode: application to the reduction of nickel, tantalum and niobium salts in fused electrolytes, J. Appl. Electrochem. 24 (1994) 361, https://doi.org/10.1007/BF00242067.
[17] L. Arurault, J. Bouteillon, J.C. Poignet, Chemical stability of solutions of niobium V in molten NaCl-KCl at 750oC, J. Electrochem. Soc. 9 (1995) 16.
[18] G.S. Picard, Niobium chemistry in molten LiCl+KCl eutectic, SAVE Proc. 1992–16 (1992) 622–631, https://doi.org/10.1149/199216.0622PV.
[19] F. Lantelme, A. Barhoun, J. Chevalet, Electrochemical behavior of solutions of niobium chlorides in fused alkali chlorides, J. Electrochem. Soc. 31 (1993) 324.
[20] M. Mohamedi, Y. Sato, T. Yamamura, Examination of niobium electrochemistry from the reduction of Nb_3Cl_8 in molten LiCl−KCl eutectic, Electrochim. Acta 44 (1999) 1559–1565, https://doi.org/10.1016/S0013-4686(98)00288-6.
[21] G.Y. Jeong, S. Sohn, Y. Jeon, J. Park, Understanding of electrochemical behaviors of niobium in molten LiCl−KCl eutectic for pyrochemical decontamination process, J. Nucl. Mater. 524 (2019) 39–53, https://doi.org/10.1016/j.jnucmat.2019.06.037.
[22] R. Fujita, H. Nakamura, Y. Haruguchi, R. Takahashi, K. Utsunomiya, M. Sato, Y. Ito, T. Goto, T. Terai, S. Ogawa, Development of a zirconium recycle process from zircaloy waste of a boiling water reactor (BWR), Trans. Atom. Energy Soc. Jpn. 6 (2007) 343–357, https://doi.org/10.3327/taesj.J06.031.
[23] K.T. Park, T.H. Lee, N.C. Jo, H.H. Nersisyan, B.S. Chun, H.H. Lee, J.H. Lee, Purification of nuclear grade Zr scrap as the high purity dense Zr deposits from Zirlo scrap by electrorefining in LiF−KF−ZrF4 molten fluorides, J. Nucl. Mater. 436 (2013) 130–138, https://doi.org/10.1016/j.jnucmat.2013.01.310.
[24] C.H. Lee, D.Y. Kang, M.K. Jeon, K.H. Kang, S.W. Paek, D.H. Ahn, K.T. Park, Addition effect of fluoride compounds for Zr electrorefining in LiCl-KCl molten salts, Int. J. Electrochem. Sci. 11 (2016) 566–576.
[25] C.H. Lee, K.H. Kang, M.K. Jeon, C.M. Heo, Y.L. Lee, Electrorefining of zirconium from zircaloy-4 cladding hulls in LiCl-KCl molten salts, J. Electrochem. Soc. 159 (2012) D463–D468, https://doi.org/10.1149/2.012208jes.
[26] S. Sohn, J. Park, I.S. Hwang, Electrolytic recovery of high purity Zr from radioactively contaminated Zr alloys in chloride salts, Int. J. Electrochem. Sci. 13 (2018) 3897.
[27] J. Hur, S. Jeong, S. Sohn, J. Park, I.S. Hwang, Separation of Zr from Zr-2.5Nb by electrorefining in LiCl-KCl for volumetric decontamination of CANDU pressure tube, Appl. Sci. 11 (9) (2021) 3790, https://doi.org/10.3390/app11093790.
[28] J. Hur, Y. Jeon, G. Jeong, S. Sohn, S. Choi, J. Park, Zirconium metal recovery from irradiated radioactive zirconium alloy via chloride-based electrorefining and thermal decomposition of ZrCl, Int. J. Energy Res. 46 (2022) 6164–6176.
[29] S.M. Bowman, I.C. Gauld, O.A. Primer, How to Perform Isotopic Depletion and Decay Calculations with SCALE/Origen, ORNL/TM-2010/43, 2010.
[30] W.K. Behl, Linear sweep voltammetry of Ni(ll), Co(ll). Cd(ll), and Pb(ll) at glassy carbon electrodes in molten lithium chloride-potassium chloride Eutectic, J. Electrochem. Soc. 118 (1971) 889, https://doi.org/10.1149/1.2408212.
[31] J. Braunstein, G. Mamantov, G.P. Smith, Advances in Molten Salt Chemistry, second ed., Springer, New York, 1973.
[32] H.A. Laitinen, C.H. Liu, An electromotive force series in molten lithium chloride-potassium chloride Eutectic, J. Am. Chem. Soc. 80 (1958) 1015–1020, https://doi.org/10.1021/ja01538a001.
[33] H.C. Eun, H.C. Yang, H.S. Lee, In Tae Kim, Distillation and condensation of LiCl−KCl eutectic salts for a separation of pure salts from salt wastes from an electrorefining process, J. Nucl. Mater. 395 (2009) 58–61.
[34] M.K. Jeon, Y.T. Choi, J.M. Hur, D.-H. Ahn, A thermo-gravimetric analysis study on the chlorination reaction of ZIRLO cladding hulls, J. Nucl. Mater. 465 (2015) 28–33.
[35] H.-C. Yang, H.-C. Eun, H.-S. Lee, Y.-J. Cho, Closed chamber salt distillation system for an enhanced recovery of evaporated pure salt, J. Nucl. Sci. Technol. 47 (11) (2010) 973–976, https://doi.org/10.1080/18811248.2010.9711661.